



FULL ARTICLE

Indocyanine green-enhanced multimodal photoacoustic microscopy and optical coherence tomography molecular imaging of choroidal neovascularization

Van Phuc Nguyen^{1,2}  | Jeff Folz³ | Yanxiu Li¹ | Jessica Henry¹ |
Wei Zhang⁴ | Thomas Qian¹ | Xueding Wang⁴ | Yannis M. Paulus^{1,4*} 

¹Department of Ophthalmology and Visual Sciences, University of Michigan, Ann Arbor, Michigan

²NTT-Hi Tech Institute, Nguyen Tat Thanh University, Ho Chi Minh, Vietnam

³Biophysics Program, University of Michigan, Ann Arbor, Michigan

⁴Department of Biomedical Engineering, University of Michigan, Ann Arbor, Michigan

*Correspondence

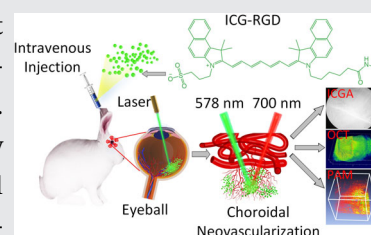
Yannis M. Paulus, Department of Ophthalmology and Visual Sciences, University of Michigan, 1000 Wall Street Ann Arbor, MI 48105, USA.
Email: ypaulus@med.umich.edu

Funding information

Fight for Sight- International Retinal Research Foundation, Grant/Award Number: FFSGIA16002 (YMP); National Eye Institute, Grant/Award Numbers: 1K08EY027458 (YMP), P30 EY007003

Abstract

Photoacoustic microscopy (PAM) has great potential for visualization of the microvasculature with high spatial resolution and contrast. Early detection and differentiation of newly developed blood vessels named choroidal neovascularization (CNV) from normal vas-



culature remains a challenge in ophthalmology. Exogenous contrast agents can assist with improving PAM sensitivity, leading to differentiation of CNV. Here, an FDA-approved indocyanine green (ICG) was utilized as a PAM contrast agent. ICG was conjugated with RGD peptides, allowing the ICG to bind to the integrin expressed in CNV. Molecular PAM imaging showed that ICG-RGD can target CNV for up to 5 days post intravenous administration in living rabbits with a model of CNV. The PAM image sensitivity and image contrast were significantly enhanced by 15-fold at 24 h post-injection. Overall, the presented approach demonstrates the possibility of targeted ICG to be employed in PAM molecular imaging, allowing more precise evaluation of neovascularization.

KEYWORDS

choroidal neovascularization, contrast agent, indocyanine green, multimodal imaging modality, optical coherence tomography, photoacoustic microscopy

1 | INTRODUCTION

The development of neovascularization and vascular abnormalities play a critical role in numerous medical diseases. For example, age-related macular degeneration (AMD) is the leading cause of irreversible vision loss in the world and will continue to increase with the aging of the population [1–3]. The major cause of vision loss in AMD is associated with the development of new microvasculature named choroidal neovascularization (CNV). While treatments exist, early detection is essential to

optimize patient outcomes. A wide variety of imaging modalities have been used to visualize CNV and understand CNV pathogenesis, including fluorescein angiography (FA), indocyanine green angiography (ICGA), optical coherence tomography (OCT), and OCT angiography (OCTA) [2, 4–7]. However, these imaging modalities each have their own limitations. For example, FA and ICGA are unable to indicate the depth of the vasculature. Although OCT and OCTA can visualize CNV and vasculature, these techniques cannot detect leakage at CNV. Therefore, there exists a need to improve visualization of

neovascularization, allowing for early diagnosis and improved treatment outcome for patients.

Photoacoustic microscopy (PAM) has been explored as a promising imaging technique to better identify the position and margins of CNV [8–10]. The advantages of PAM include that it is non-invasive, high resolution, high contrast, and has a deeper penetration depth than strictly optical techniques such as confocal or OCT. This technique has been performed to visualize different retinal anatomy such as the retinal pigment epithelium (RPE), melanin, retinal vessels, choroidal vessels, choroidal neovascularization, retinal neovascularization, and corneal neovascularization as well as functional information such as oxygen saturation [11–13]. To better detect CNV, PAM imaging can be integrated with other optical imaging modalities such as OCT, fluorescence microscopy, and scanning laser ophthalmoscopy (SLO). Xiao et al and Zhang et al have described a combination of PAM, OCT, and FM system for visualization of CNV, melanin, and retinal anatomy in mice and rats with high resolution [14, 15]. However, these studies could not distinguish CNV from the surrounding blood vessels. In addition, these studies were performed in small animals, resulting in limited clinical translatability due to the axial length of the eye of rats and mice being much smaller than that of the axial length of human eye. For example, the axial length of rats is ~6 mm, and mice are ~3 mm versus the axial length of human eye is about 23 mm [16–19]. To address such limitations, our group has successfully developed an integrated PAM and OCT system for larger animal eyes. This integrated multimodality imaging utilizes the benefits of each system to give more information. Based on optical scattering, OCT offers high contrast and high resolution imaging of different retinal layers, including the internal limiting membrane, retinal nerve fiber layer, ganglion cell layer, inner plexiform layer, inner nuclear layer, outer plexiform layer, outer nuclear layer, external limiting membrane, photoreceptor layer, ellipsoid zone, retinal pigment epithelium, choriocapillaris, choroid, and newly developed choroidal neovascularization (CNV) in pathologic states, which is not possible to visualize with PAM alone [8, 20–26]. By using the selected PAM wavelength of incident light (i.e., $\lambda = 578$ nm), which has a strong optical absorption of hemoglobin, PAM can selectively image the blood vessels even with the preretinal fibrovascular membrane above the retinal blood vessels. With its selective absorption, PAM is not sensitive to the different retinal layers, which appear on OCT, and instead allows for improved visualization of hemoglobin and melanin. In previous studies, our group has shown that the multimodality PAM and OCT system could achieve in vivo label-free determination of retinal and choroidal vessels in rabbits

with high resolution and contrast. The retinal structural information obtained by PAM imaging is consistent with the information acquired by OCT, demonstrating the feasibility of multimodal imaging for accurate visualization of the retina's complex vascular network. This multimodal imaging system has also been utilized to perform label-free imaging of abnormal retinal vessels in living rabbits such as retinal neovascularization, retinal vein occlusion, laser-induced injury, and subretinal injection of VEGF-induced choroidal neovascularization [10, 21, 23–28]. One limitation of these studies is that it is difficult to distinguish neovascularization from native vessels due to overlapping strong absorption of hemoglobin within blood vessels. Semi-automatic segmentation has been applied to classify native vessels and neovascularization, resulting in imprecise identification of the margins of the abnormal vessels. Therefore, to better visualize newly developed blood vessels and improve the capability of distinguishing individual vessels, near-infrared (NIR; 650–1000 nm) exogenous contrast agents can be applied because hemoglobin has low absorption of the excitation laser light at that wavelength, resulting in low intrinsic endogenous photoacoustic signal.

Several NIR contrast agents have been investigated for PA imaging to improve visualization of biological tissues and can be classified into two groups: organic and inorganic materials. Inorganic PA contrast agents such as gold nanoparticles (including star, rod, sphere, and wire), silica [29, 30], single-wall carbon nanotube [31, 32] and copper sulfide nanoparticles [33, 34] have shown an excellent PA image contrast in many biomedical applications such as cancer, inflammation, bone, and eyes [35–39]. Long-term toxicity concern is a major challenge of inorganic contrast agents, and many have not been approved by the US Food and Drug Administration (FDA) for clinical use. In contrast, organic dyes such as methylene blue, porphyrin, NIR780, melanin, Cy5, cyanine-based dyes, perylene-diimide (PDI), naphthalocyanines, phthalocyanine, Prussian blue, astaxanthin, indocyanine green (ICG), fluorescent reporter genes, and semiconductor polymers have been utilized in PA imaging due to their excellent biodegradability and biocompatibility [39–43]. The use of reporter genes as genetically encoded exogenous PA contrast would provide further chance to understand more complex biological behaviors such as cell growth dynamics, gene expression, and signaling. A study reported by Jathoul et al. has demonstrated that tyrosinase-based PA genetic reporters provide high-resolution imaging of genetically labeled cells in three dimensions at a depth up to 1 cm, as well as long-term visualization of cell growth over a period of 52 days [40]. However, PA genetic reporters are associated with potentially toxic

effects due to singlet oxygen generation during protein maturation, complicated processing, and high costs. Currently, it is still not approved by the FDA for clinical application. ICG is among the few NIR PA contrast agents approved by the FDA for clinical application. ICG demonstrates high optical absorption and high PA contrast as evaluated in lymph nodes or in tumors in vivo [44]. ICG has been approved and widely used in ophthalmology to visualize choroidal vasculature [45]. To date, no study has used ICG for improving PAM signal in eye applications.

This study evaluates the biocompatibility, biostability, and photostability of functionalized ICG with specific targeting RGD peptides (ICG-RGD) as a PAM contrast agent to visualize choroidal neovascularization (CNV) in living rabbits. By conjugation with RGD peptides, the synthesized ICG-RGD can target $\alpha_v\beta_3$ integrin or other molecules expressed in CNV, enabling the identification and determination of the location and margins of CNV from the surrounding retinal blood vessel network with exceptional contrast, penetration depth, and visualization in three dimensions. Along with PAM imaging, the characterization of CNV was evaluated using color fundus photography, FA, and OCT before and after injection of ICG-RGD intravenously. The use of low excitation laser energy of 80 nJ (50% of the ANSI safety limit) allows for long-term visualization of CNV with a high spatial resolution due to reduced photobleaching and photodegradation. We demonstrate this by imaging CNV in rabbits before and after administration of targeted ICG-RGD over a period of 14 days using PAM imaging at various excitation wavelengths. The integration of high resolution, high image contrast, and stability of ICG-RGD molecular PAM imaging provides an important step for the visualization of CNV.

2 | MATERIALS AND METHODS

2.1 | Synthesis of ICG conjugation with RGD peptide

A total of 5 mg of indocyanine green succinimidyl ester (ICG-NHS) was dissolved in 100 μ L of DMSO. This solution was added to 900 μ L of pH 7.4 PBS solution containing 10 mg of Arginyl-glycyl-aspartic acid (RGD) peptide. This reaction was stirred for 4 hours, at which time the solution was diluted to 20 mL with Millipore water. The unreacted ICG-NHS, which is water insoluble, was then centrifuged out of solution (10 min, 4000RPM). The supernatant was then collected and washed several times with a 3 kDa Amicon Centrifuge Filter to remove

any salts. The solution was then lyophilized for 48 hours to yield a green powder, ICG-RGD.

2.2 | Characterization of ICG-RGD contrast agent for PAM

The optical properties ICG-RGD were analyzed and evaluated. The absorption spectrum of ICG-RGD was determined from 400 to 1000 nm by ultraviolet-visible (UV-Vis) spectroscopy (UV-3600, Shimadzu Corp., Japan) to select the optimal excitation wavelength for PAM imaging. Stability of the synthesized ICG-RGD was evaluated using UV-Vis spectroscopy analysis at different time points: 1 week, 2 weeks, and 1 month.

3 | CYTOTOXICITY ASSESSMENTS

3.1 | Cell culture

HeLa and human retinal pigment epithelium (ARPE-19) cells were cultured in 100-mm tissue culture dishes. Complete DMEM and DMEM/F12 were prepared by added with 10% fetal bovine serum (FBS), 1.18 g sodium bicarbonate, and 10 mL antibiotics/antimycotics. The cells were incubated at 37°C in humidified atmosphere of 5% CO₂ and 95% air. When the cells reached 70% to 90%, they were isolated by adding 1 mL of 0.25% trypsin-EDTA. The trypsinized cells were then centrifuged at 500 rpm for 5 min.

3.2 | Cytotoxicity of ICG-RGD

Cytotoxicity of ICG-RGD was tested on HeLa and ARPE-19 cells. The cells were seeded in 96-well plates at a density of 10⁴ cells/well and incubated for 24 hours at 37°C and 5% CO₂. Then, the cells were treated with ICG-RGD at various final concentrations (i.e., 0.5, 12.5, 25, 50, 100, 200, and 400 μ g/mL). Untreated cells were used as control. The cells were further incubated for 24 and 48 hours. A standard methyl tetrazolium (MTT) assay was used to determine the percentage of viable cells.

3.3 | Apoptosis analysis

To further evaluate the potential apoptosis induced by ICG-RGD, flow cytometry analysis was carried out using an Annexin-V FITC Apoptosis Detection Kit. Briefly, cells were harvested incubated with ICG-RGD at

concentration of 0.16 mg/mL for 24 and 48 hours. Then, the cells were re-suspended in mixed 500 μ L 1 \times buffer binding with 5 μ L (10 μ g/mL) of Annexin-V FITC and PI solution and kept at room temperature in dark place for 15 min. The stained cells were diluted with 1 mL of cold PBS for flow cytometer analysis. In addition, three negative control samples were also prepared. Half of the control cells were incubated in water bath at 56°C for 5 min. These cells were mixed with the remaining cells and gently pipetted a few times. The cells were then split into three different sub-samples and stained with FITC only, PI only, and unstained cells with PI and FITC. All prepared samples were analyzed with a flow cytometer within 1 h to avoid systemic error caused by cell death. The analysis provided the degrees of viability, early apoptosis, late apoptosis and necrosis information in four quadrants: Lower left portion (Q1) indicated viable cells (Annexin - V⁻/PI⁻); lower right (Q2) denotes early apoptotic cells (Annexin - V⁺/PI⁻), upper right (Q3) is late apoptotic cells (Annexin - V⁺/PI⁺), and upper left (Q4) represents necrotic cells (Annexin - V⁻/PI⁺).

3.4 | Cellular uptake

To observe intracellular uptake of ICG-RGD, treated cells with ICG-RGD were imaged using confocal microscopy. The cells were cultured in 35 mm μ -plates at a density of 2×10^5 cells/well and incubated at 37°C and 5% CO₂ for 24 h. Then, the cells were then treated with ICG-RGD at various final concentrations (i.e., 25, 50, and 100 μ g/mL) and incubated for 24 and 48 hours. Afterwards, the treated cells were washed with cold PBS three times and fixed with formaldehyde at a concentration of 2.5% for 30 min. The fixed cells were then stained with Hoechst 33342 (300 μ L, 10 μ g/mL) for 20 min. The sample was washed with PBS two times and imaged using confocal SP5 laser scanning microscope.

3.5 | Phantom preparation

A group of six mimicking silicone phantom tubes (inner diameter = 0.30 mm and outer diameter = 0.64 mm) was prepared to test the feasibility of PAM signal of ICG-RGD. The tubes were poured with ICG-RGD solution at different concentrations (i.e., 0 [saline], 0.01, 0.02, 0.04, 0.08, 0.16 and 0.32 mg/mL). Another set of phantom samples including one tube filled with blood and 1 tube filled with mixed blood and ICG-RGD at a final concentration of 0.04 mg/mL was prepared to compare the

photoacoustic signal between blood and ICG. Both the distal ends of each tube were sealed with optical adhesive.

3.6 | Animal model preparation and CNV models

The University of Michigan's Institutional Animal Care and Use Committee (IACUC) (PRO00008566, PI: Y.M. Paulus) approved the experimental protocols, and all animal experiments were performed in compliance with the principles and guidelines of the Association for Research in Vision and Ophthalmology (ARVO) Statement on the Use of Laboratory Animals in Ophthalmic and Vision Research.

Six New Zealand white rabbits with an age of 2–8 months and weight of 2.2–2.8 kg, both genders, were obtained by generous donation from the Center for Advanced Models and Translational Sciences and Therapeutics (CAMTraST) at the University of Michigan Medical School. The rabbits were kept in an air-conditioned room with a 12-h light–dark cycle, free access to water, and fed standard laboratory food. Subretinal injection of Matrigel and VEGF-165 was performed to create choroidal neovascularization (CNV) model as described in detail previously [10]. Briefly, a mixed solution of human vascular endothelial growth factor VEGF-165 (Shenandoah Biotechnology, Warwick, USA) and Matrigel basement membrane matrix (Corning, NY, USA) was prepared. VEGF-165 was stabilized in 1% bovine serum albumin at concentration of 0.1 mg/mL in stock solution. Then, 750 ng VEGF at concentration of 100 μ g/mL was suspended with 20 μ L of Matrigel.

The rabbits were anesthetized by intramuscular injection of a mixed solution of ketamine (40 mg/kg, 100 mg/mL) and xylazine (5 mg/kg, 100 mg/mL). To maintain adequate anesthesia, a vaporized isoflurane anesthetic (1 L/min oxygen and 0.75% isoflurane) (Surgivet, MN, USA) was employed in combination with possible additional injections of ketamine (~1/3 dose every 45 min) during the experimental procedures to maintain animal anesthesia. To dilate the rabbit's pupils, a drop of tropicamide 1% ophthalmic and phenylephrine hydrochloride 2.5% ophthalmic were applied. 0.5% proparacaine hydrochloride ophthalmic solution was added in the eye for topical local anesthesia. Two to three drops of eye drop solution (Systane, Alcon Inc., TX, USA) was provided every minute to avoid corneal dehydration and to maximize the coupling between laser light and ultrasound transducer. During the experiment and

recovery, the rabbit's vital signs, such as body temperature, mucus mucous membrane color, temperature, heart rate, and respiratory rate, were monitored and recorded every 15 minutes.

3.7 | In vivo PAM imaging of choroidal neovascularization in rabbit

The location and margin of choroidal neovascularization (CNV) were assessed using multimodal imaging: color fundus photography, fluorescein angiography (FA), indocyanine green angiography (ICGA), and integrated PAM and OCT before and after administration of ICG-RGD at various time points, including 2, 4, 24, 48, 72 hours, and days 5, 7, 9, and 14. Color fundus photography, FA, and ICGA images were acquired to visualize the retinal vessel network, the development of CNV, and to determine the scanning area for PAM and OCT. Color fundus photography, FA, and ICGA images were acquired using the Topcon 50EX camera (Topcon Corporation, Tokyo, Japan). FA and ICGA images were acquired immediately after taking color fundus photographs. A dose of 200 μ L (10%) sodium fluorescein solution (Akorn, Lake Forest, IL, USA) was intravenously injected into the rabbit marginal ear vein. The FA images were immediately acquired, and late phase FA images were captured every minute for at least 15 minutes. Non-conjugated control ICG images before the injection of ICG-RGD were also acquired by intravenous injection of 200 μ L ICG solution at concentration of 2.5 mg/mL. The ICGA images were acquired using excitation and emission filters of 782 nm and 820 nm, respectively, on the Topcon 50EX camera. These ICGA images were obtained using the same exposure light intensity (ISO = 5000, Aperture = 2.5, flash = 300) and the fluorescent intensity was determined using ImageJ analysis.

After taking fundus, FA, and ICGA images, baseline PAM and OCT images of CNV were obtained using a multimodal custom-made PAM and OCT imaging system. The body and head of the rabbit were placed on two different stabilization XYZ linear stages to allow for free adjustment of the scanning area and to avoid motion artifacts. The selected scanning areas were imaged with the OCT imaging system. Then, PAM images were acquired at 578 nm and 700 nm before and after intravenous administration of 0.4 mL ICG-RGD (2.5 mg/mL) at various time points: 2, 4, 8, 24, 48, 72 hours, and days 5, 7, 9, and 14 post-injection to visualize ICG-RGD at CNV. The PAM images were acquired under laser excitation energy \sim 80 nJ at 578 and 700 nm. The PA signal amplitude was quantified by using region of interest (ROI) analysis using MATLAB software (Figure S5). To

minimize the systemic error, dozens of positions were randomly selected on the PAM image to determine PAM amplitude. Biosafety was evaluated on all treated rabbits by monitoring body weights daily for 14 days. The acute toxicity was further assessed by performing histology, TUNEL assay, liver, and kidney function tests. In addition, to enhance evaluation of CNV, 3D volumetric image rendering was conducted using the Amira software.

3.8 | Multimodality PAM and OCT imaging equipment

A custom-built multimodality PAM and OCT system (Figure S1) was described in detail in previous studies [24]. In brief, a tunable excitation nanosecond pulsed laser light (3 ~ 5 ns) with a pulse repetition rate of 1 kHz pumped by diode solid-state laser (NT-242, Ekspla, Vilnius, Lithuania) was used as the PA light source. The excitation wavelength can be adjusted from 405–2600 nm, allowing for spectroscopic PA images. The excitation laser energy is estimated to be 80 nJ at the cornea, which is about half of the ANSI safety limit (i.e., \leq 160 nJ at 570 and 700 nm) [24, 46]. The use of low laser energy allows one to avoid thermoacoustic damage of the retina as described by Delori et al. [47, 48]. The collimated laser light passed through a telescope consist of two components scan lens ($f = 36$ mm, OCT-LK3-BB, Thorlabs, Inc., Newton, NJ) and an ophthalmic lens ($f = 10$ mm, AC080-010-B-ML, Thorlabs). Then, the light with a beam diameter of approximately 2 mm was delivered through the cornea and penetrated through the rabbit optics and focused on the fundus with an estimated retinal diameter of 20 μ m. An ultrasound detector with a center wavelength of 27.0 MHz (two-way bandwidth \sim 60%) was selected to detect the laser-induced PA signal (Optosonic Inc., Arcadia, CA, USA) [49]. The generated analog PA signal was first amplified by a low-noise amplifier (gain 57 dB, AU-1647, L3 Narda-MITEQ, NY) and then converted from analog into digital signal using a 200 MHz digitizer (PX1500-4, Signatec Inc., Newport Beach, CA). The lateral and axial resolutions at the focal plane of the scan lens were estimated to be 4.1 and 37.0 μ m, respectively. By raster scanning along the x- and y-axes using an optical-scanning galvanometer, three-dimensional volumetric PA images were obtained and rendered using the Amira software. In addition, to enhance visualization of CNV, the PAM images acquired at multiple wavelengths were co-localized on the same orthogonal image planes. The margins of CNV were determined using image segmentation algorithm by using Matlab 2019b (MathWorks, USA). The estimated area was measured by ImageJ software (ImageJ, NIH, USA).

OCT images before and after the injection of ICG-RGD were obtained using Ganymede-II-HR OCT system (Thorlabs, Newton, NJ) with modification. Briefly, an optical ocular lens was added into the system under an optical scan lens, and dispersion compensation glass was added into the reference arm as shown in Figure S1 [24]. To induce OCT signal, two super luminescent diodes with center excitation wavelength of 846 nm and 932 nm were used to illuminate the samples. The system can achieve A-line scan rate of 36 kHz with scan angle $\pm 10.6^\circ$. The axial and lateral resolution are 5.0 and 3.8 μm , respectively. These resolutions were determined using the full-width at half-maximum (FWHM). The OCT and PAM excitation light were coaxially aligned, enabling multimodal imaging. B-scan OCT images were acquired with resolution of 512 pixels with A-scan density of 1024 A-lines.

3.9 | Histological, TUNEL assay and immunostaining analysis

To assess the development of CNV as well as the potential toxicity of the synthesized ICG-RGD to the eye, histological analysis, and TUNEL assay were implemented for all the treated rabbits. The rabbits were euthanized at day 14 post-injection by intravenous injection of euthanasia solution (0.22 mg/kg) (Beuthanasia-D Special, Intervet Inc., Madison, NJ, USA). The whole eye was isolated and fixed with Davidson's fixative solution (Electron Microscope Sciences, PA, USA) for 24 hours at room temperature. Then the samples were washed with 50% alcohol solution (Fisher Scientific, PA, USA) for 8 hours and 70% alcohol solution for 24 hours. Fixed sample were sectioned into 5–6 mm rectangular segments, embedded in paraffin, and sectioned into a thickness of 6 μm serially using a Leica autostainer XL (Leica Biosystems, Nussloch, Germany). For histopathological analysis, the sectioned samples were stained with hematoxylin and eosin (H&E). For TUNEL assay, the samples were processed in accordance with TUNEL in situ Cell Death Detection Kit protocol (Sigma-Aldrich, USA). To visualize the formation of CNV, single immunohistochemistry slides were stained with anti-alpha smooth muscle actin (α -SMA) antibody to stain smooth muscle cells in vessel walls (Abcam, Burlingame, CA, US). All stained samples were observed using DM6000 microscope and digital images were captured using the BF450C camera (for H&E) and the FF363x camera (for TUNEL) (DM600, Leica Biosystems, Nussloch, Germany).

4 | RESULTS

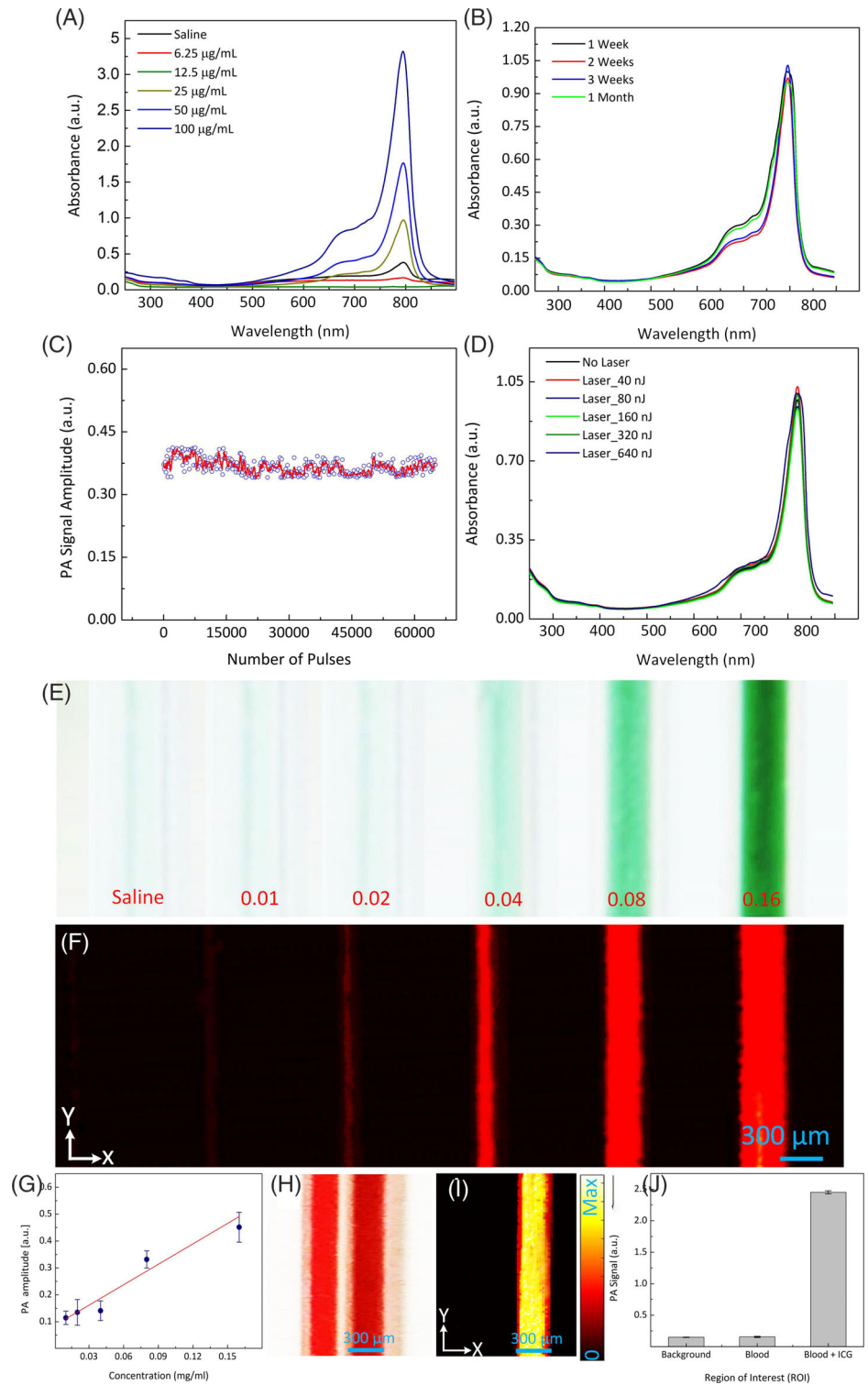
4.1 | Characterization and in vitro evaluation of the targeting ICG contrast agents

Functionalized ICG-RGD were synthesized and characterized. The absorption spectrum of ICG-RGD was measured using ultraviolet–visible (UV–Vis) spectroscopy. Figure 1A exhibits the UV–Vis absorption spectrum of ICG-RGD obtained at various concentrations (i.e., 0 [saline], 6.25, 12.5, 25, 50, and 100 $\mu\text{g}/\text{mL}$). As expected, the absorption spectrum exhibits peak absorption of ICG-RGD at 780 nm. The optical absorption increases with the concentration of ICG-RGD. To evaluate the temporal stability of ICG-RGD, the absorption spectrum of the sample was measured at different times over a period of 1 month. Figure 1B shows that the absorption spectrum did not change over a period of 4 weeks, indicating that ICG-RGD shows temporal stability and is suitable for long term evaluation in vivo. To evaluate potential photobleaching during in vivo experiments, the photostability was tested on the samples by illuminating the sample with 65 000 short laser pulses at different laser energies (i.e., 40, 80, 160, 320, and 640 nJ). As shown in Figure 1C, the PA signal was stable during laser irradiation at a wavelength of 700 nm. In addition, the absorption spectrum changed less than 2% even at high laser energies, verifying the photostability of ICG-RGD (Figure 1D).

In vitro PAM analysis was examined in a phantom to test the feasibility of ICG-RGD as a PAM contrast agent. Figure 1E exhibits a photograph of silicone tubes with an inner diameter of 300 μm filled with different concentrations of ICG-RGD (i.e., 0.01, 0.02, 0.04, 0.08, and 0.16 mg/mL). Figure 1F shows the corresponding PAM images acquired at an excitation wavelength of 700 nm. Samples with ICG-RGD at a concentration of 0.16 mg/mL were clearly visible on the PAM image with high signal. In contrast, sample with the lowest concentration of ICG-RGD (0.01 mg/mL) had very weak signal. Figure 1G shows a graph of the measurement PA signal as a function of ICG concentration. This shows a linear relationship between PA signal versus the concentration of ICG ($R^2 = 0.995$). At the highest concentration of ICG, the PAM signal increased by 35-fold from 0.013 ± 0.001 a.u. for background to 0.45 ± 0.06 a.u. for 0.16 mg/mL whereas the PA signal increased about 9-fold at the lowest concentration of ICG ($\text{PA}_{\text{signal}} = 0.11 \pm 0.02$ a.u. for 0.01 mg/mL). The lowest detectable concentration is 0.01 mg/mL with a signal to noise ratio (SNR) of 9.27 dB. To assess the image contrast enhancement in blood vessels, two mimicking phantom samples were prepared as

FIGURE 1 Optical

Characterization of indocyanine green (ICG)-RGD: A, UV-Vis absorption spectrum of ICG-RGD measured from different concentrations (i.e., 0 [saline], 6.25, 12.5, 25, 50 and 100 µg/mL). B, Stability of ICG-RGD evaluated by measuring UV-Vis absorption spectrum at different times (i.e., 1, 2, 3 weeks, and 1 month). C, Photostability of ICG-RGD phantom sample at a concentration of 0.08 mg/mL under 65 000 short pulsed laser irradiation. D, Absorption spectra of the sample after laser irradiation at different energies from 0 to 640 nJ, demonstrating photostability of ICG-RGD. E, Photograph of silicone tube phantoms filled with ICG-RGD at different concentrations ranging from 0 (saline) to 0.32 mg/mL. F, Corresponding maximum intensity projection (MIP) photoacoustic microscopy (PAM) image acquired at 700 nm. G, Graph of measured PA amplitudes using regions of interest (ROI) analysis. The PA amplitudes linearly increase with the increase in ICG concentration ($R^2 = 0.99$). H, Photograph of the samples filled with fresh rabbit blood and mixed blood and ICG at a final concentration of 0.04 mg/mL. I, PAM image acquired at 700 nm. The sample poured with blood only was not visible on PAM image. J, Comparison of PA signal isolated from three different locations in PAM images, including background, blood, and mixed blood and ICG-RGD



shown in Figure 1H. The samples were filled with fresh rabbit blood and mixed blood with ICG-RGD at a final concentration of 0.04 mg/mL. Figure 1I shows the corresponding PAM image acquired at an excitation wavelength of 700 nm. The image contrast of the sample filled with blood and ICG showed excellent contrast due to strong absorption of ICG at that wavelength. In contrast, the sample filled with blood was

not visible on PAM due to low optical absorption of hemoglobin at 700 nm. By using region of interest (ROI) analysis (Figure 1J), the PAM image contrast significantly increased and achieved 17.5-fold higher than that of background and blood sample (i.e., $PA_{\text{signal}} = 2.45 \pm 0.02$ a.u., 0.16 ± 0.01 a.u., and 0.14 ± 0.01 a.u. for blood+ICG, blood, and background, respectively).

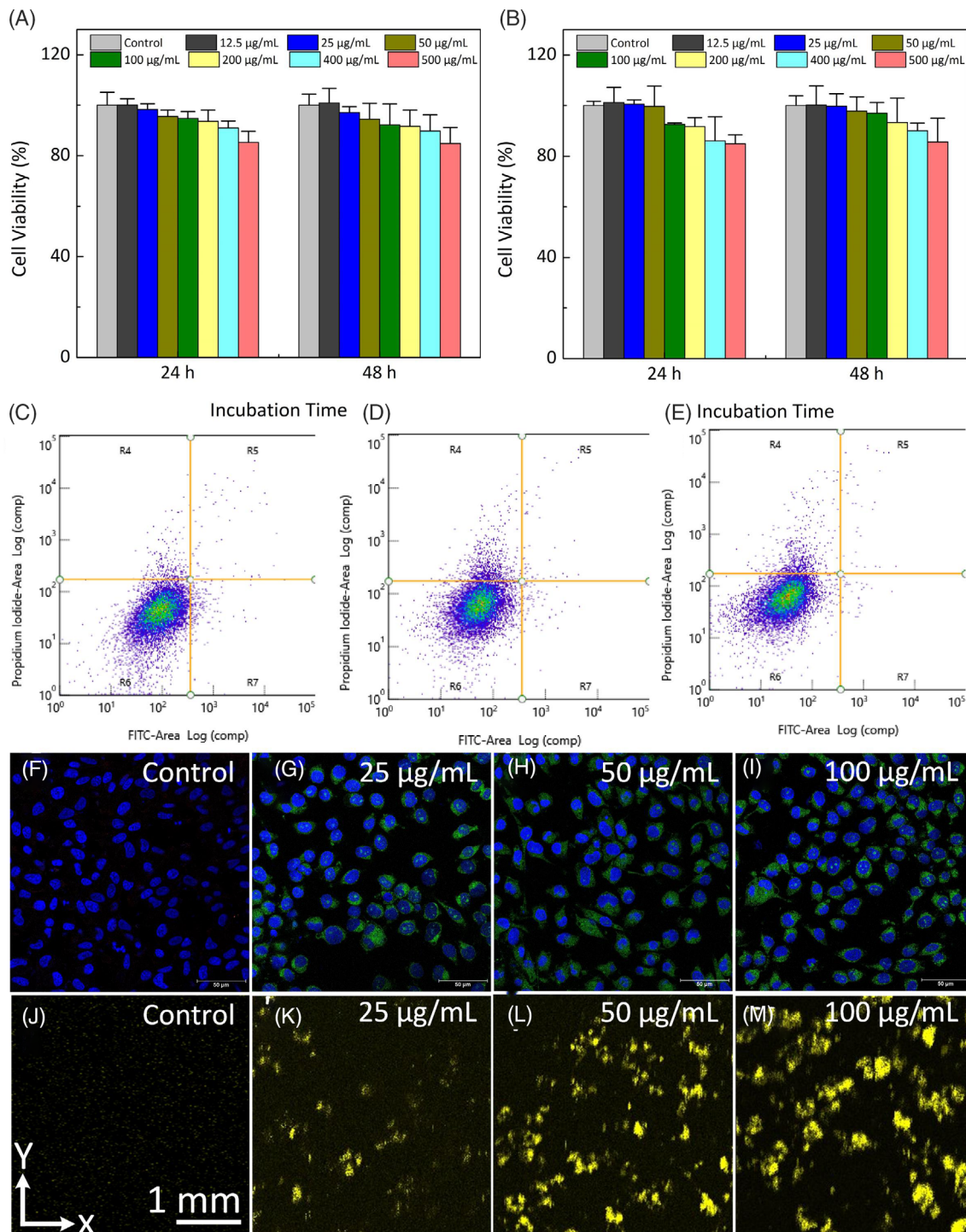


FIGURE 2 Cytotoxicity, cellular uptake, and in vitro single cell visualization. A–B, Cytotoxicity of ICG in HeLa and ARPE-19 cells. Cells were treated with ICG at different concentrations ranging from 0 to 500 $\mu\text{g}/\text{mL}$ and various incubation times (24 h and 48 h). Data are presented as mean and standard deviation, $N = 4$. C–E, Flow cytometry analysis on ARPE-19 cells treated with ICG at concentration of 200 $\mu\text{g}/\text{mL}$. F–I, Cellular uptake of ICG. Cells were incubated with ICG at various concentrations (0 (control), 25, 50 and 100 $\mu\text{g}/\text{mL}$) for 24 h. Pseudo-green color indicate the ICG internalized in cells. J–M, Evaluation of in vitro PAM imaging for single cell detection. Cells were imaged with an excitation wavelength of 700 nm and laser energy of 80 nJ. The cells treated with ICG-RGD at a concentration of 100 $\mu\text{g}/\text{mL}$ showed higher contrast when compared with lower concentrations of ICG

4.2 | In vitro cytotoxicity and cellular uptake of ICG-RGD contrast agents

To assess any potential cytotoxicity of ICG-RGD, MTT assay, flow cytometry, and confocal microscopy analysis were implemented on HeLa cells and human retinal pigment epithelium cells (ARPE-19) cells. Figure 2A,B exhibits the viability of HeLa and ARPE-19 cells treated with ICG-RGD at different concentrations and incubation times. Untreated cells demonstrated no change in cell viability for most concentrations and incubation times. The cell viability was slightly reduced when treated at a high concentration of ICG-RGD and long incubation time of 48 hour. For example, the survival rate of the treated cells at 400 $\mu\text{g}/\text{mL}$ was 95.9% and 96.5% cell viability for HeLa and ARPE-19 cells, respectively, after incubation for 48 hour. Next, fluorescence-activated cell sorting analysis was performed to evaluate any positive effect of ICG-RGD in inducing apoptosis of the cultured HeLa and ARPE-19 cells (Figure 2C-E). Both HeLa and ARPE-19 cells were incubated with ICG-RGD for 24 and 48 hour followed by apoptosis quantification using Annexin-V/PI analysis. All samples show slight increase in apoptosis above the control level (Total apoptosis = 1.07% for 24 h and 1.67% for 48 h for HeLa cells, 2.6% for 24 h and 1.6% for 48 h for ARPE-19 cells, 0.6% for 24 h and 1.06% for 48 h for control), demonstrating that ICG-RGD induced a negative impact on both cancer cells and retinal cell lines.

Figure 2F-I shows the intracellular uptake of ICG-RGD into HeLa and ARPE-19 cells monitored by confocal microscopy. Green fluorescent color indicates the distribution of ICG-RGD inside the cells. In contrast, no fluorescent signal was observed in untreated cells. The dye significantly accumulated in the cells when the cells were treated with higher concentration of dyes. The cells demonstrated excellent cellular uptake of ICG dye at a concentration of 100 $\mu\text{g}/\text{mL}$. The blue fluorescence color specifies cell nuclei stained by Hoechst 33342.

Intracellular uptake of ICG-RGD was further imaged in cells using a custom-built PAM and OCT imaging system to evaluate the efficiency of ICG-RGD in targeting integrins, which are expressed in neovascularization. The internalized ICG-RGD in cells were differentiated from the background using PA imaging at 700 nm as shown in Figure 2j-m. The distribution of ICG-RGD and cell density were clearly visible on the PAM image with excellent contrast at a concentration of 100 $\mu\text{g}/\text{mL}$ due to strong absorption of ICG. In contrast, few cells were visualized on the sample treated with ICG at the lowest concentration of 25 $\mu\text{g}/\text{mL}$. The PAM signal linearly increased with internalized ICG-RGD concentration and exhibited 14.2 and 1.4-fold higher signal than that of background and

lower concentration (i.e., $PA_{\text{signal}} = 1.85 \pm 0.05$ a.u. for 100 $\mu\text{g}/\text{mL}$ vs $PA_{\text{signal}} = 0.13 \pm 0.02$ a.u. for background, and $PA_{\text{signal}} = 1.34 \pm 0.06$ a.u. for 25 $\mu\text{g}/\text{mL}$).

4.3 | In vivo PAM imaging visualization of CNV

In vivo evaluation of ICG-RGD as a PAM molecular contrast agent was assessed in an animal model of CNV in living rabbits ($N = 6$) via subretinal injection of Matrigel and VEGF-165 using a custom-built multimodal PAM and OCT system (Figure S1). This imaging system can be used for imaging larger eyes. This is an important step towards clinical translation because the rabbit eye has the axial length that is similar to that of a human eye (i.e., axial length = 18 mm for the rabbit eye vs. ~23 mm for the human eye). The system provides a lateral resolution of 4.1 for PAM and 3.8 μm for OCT and axial resolution of 37.0 μm for PAM and 4.0 μm for OCT. The high resolution allows visualization of individual capillaries and neovascularization. In addition, by using an optical galvanometer scanning method, the three-dimensional volumetric PAM image can be achieved within 1 minute with a resolution of 256×256 pixels.

A group of six rabbits received subretinal injection of Matrigel and VEGF-165 and developed CNV by day 28. Multimodal imaging was obtained before the administration of ICG-RGD and post-injection. Afterwards, a dose of 400 μL of ICG at concentration of 2.5 mg/mL was intravenously injected into the rabbit via the marginal ear vein. Figure 3 shows color fundus photography, ICG, and OCT before and after administration of ICG-RGD at different time points: 1, 2, 4, 24, 48, 72 h, days 5, 7, 9, and 14 post-injection. The fundus photography shows the retinal vessels' morphology, including retinal and choroidal vessels and capillaries (Figure 3A). At the site of injection of VEGF and Matrigel (white arrows), the morphology of the choroidal vessels was significantly altered due to the effect of the Matrigel and VEGF. This is consistent with previous results by Petrus-Reurer et al. The authors have reported that subretinal injection might affect photoreceptor and induced retinal pigment epithelium degeneration, leading to dynamic changes of the vessel network [50]. Figure 3B shows the ICG imaging acquired at different times to monitor the distribution of ICG-RGD. The ICG image highlights the developed CNV through the leakage at choroidal vessels (white arrows). The location of CNV is visualized at 24 hour post-injection due to increased leakage at that time. There was no fluorescent signal observed at day 7 post-injection, suggesting that the fluorescent dye was likely cleared from the body. In contrast, CNV was only visualized by ICGA imaging

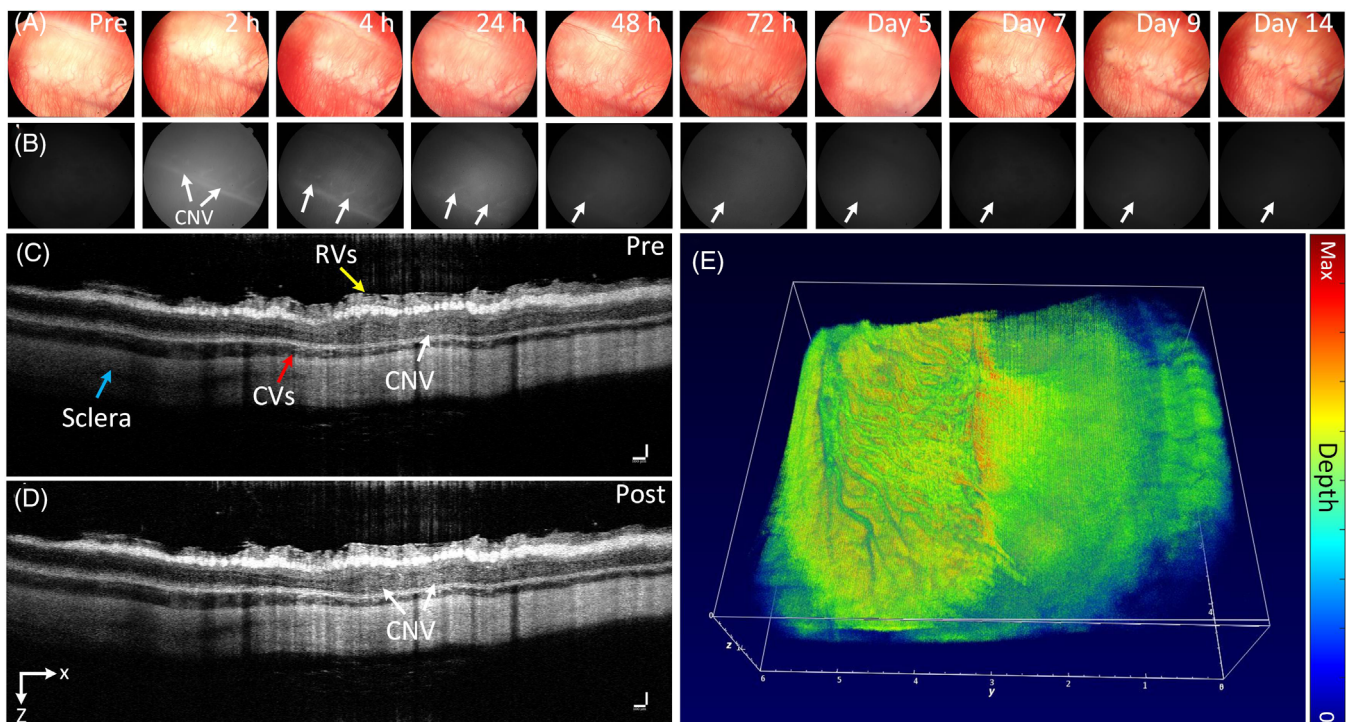


FIGURE 3 Fluorescence imaging for detection of choroidal neovascularization (CNV): A, Color fundus photography, fluorescence images of CNV before and after injection of ICG-RGD over a period of 14 days. Color fundus shows the morphology of retinal, choroidal vessels, and optic nerve. B, Fluorescence images of CNV obtained after administration of 400 μ L ICG conjugated with RGD (2.5 mg/mL). The strongest fluorescent signal was observed at 24 h post-injection. C and D, B-scan OCT images pre- and post-injection. The white arrows indicate the location of CNV, yellow arrow shows the position of retinal vessels (RVs), and turquoise arrow is sclera layer. Noted that the position of CNV after the injection shows higher contrast in comparison with before the injection. E, 3D volumetric OCT image. The encoded-color shows 3D depth information

within 15 min after the injection of unconjugated ICG solution (Figure S2) due to rapid clearance from the body. Figure 3C,D reveals the cross-sectional B-scan OCT images obtained from the selected scanning line displayed on Figure 3A. These B-scan OCT images show the retinal layers, including the ganglion cell layer (GCL), RPE, choroid, and sclera. Particularly, the position of CNV was noted to be between choroidal vessels and RPE and estimated to be $\sim 300 \mu\text{m}$ from the retinal vessels. *in vitro* OCT testing shows that ICG provided strong OCT signal at the tested concentration of ICG from 1.25–2.5 mg/mL (Figure S3). However, the OCT signal generated by ICG was not significantly increased post-injection in rabbits, possibly due to the high intrinsic retinal OCT signal, low scattering properties of the dye, dilute concentration, and/or strong scattering of leakage at the CNV site. Figure 3E shows a 3D volumetric OCT images. The retinal and choroidal vessels were clearly observed and laid at different layer (pseudo-depth color), resulting in improved visualization of the change of retinal morphology.

Longitudinal PAM observation of CNV was performed over a period of 14 days as shown in Figure 4.

The PAM images were obtained at two different optical excitation wavelengths of 578 and 700 nm. The excitation of 578 nm was used to image the anatomic structure of retinal vasculature and CNV given hemoglobin absorption at 578 nm, whereas the excitation of 700 nm was used for imaging of ICG to perform molecular imaging of CNV. Figure 4A-C exhibits overlay three-dimensional visualization of the acquired PAM data and maximum intensity projection (MIP) PAM images achieved at the excitation wavelengths of 578 and 700 nm at 24 hour post-injection. These images reveal the position and margin of CNV with great contrast compared to the optical absorption of the surrounding retinal microvasculature. The CNV was particularly distinguished at a depth of $\sim 300 \mu\text{m}$ by acquiring PAM at 700 nm where the oxygenated hemoglobin has a significantly lower PA signal. Figure 4D-F shows PAM acquired at different time points at 578 and 700 nm to evaluate longitudinal imaging of ICG. No image contrast was observed on the PAM acquired at 700 nm before the injection of ICG or post-injection of ICG from day 7 to day 14. In contrast, the biodistribution of ICG at CNV was visualized post-injection. The highest contrast was achieved at 24 hour post-

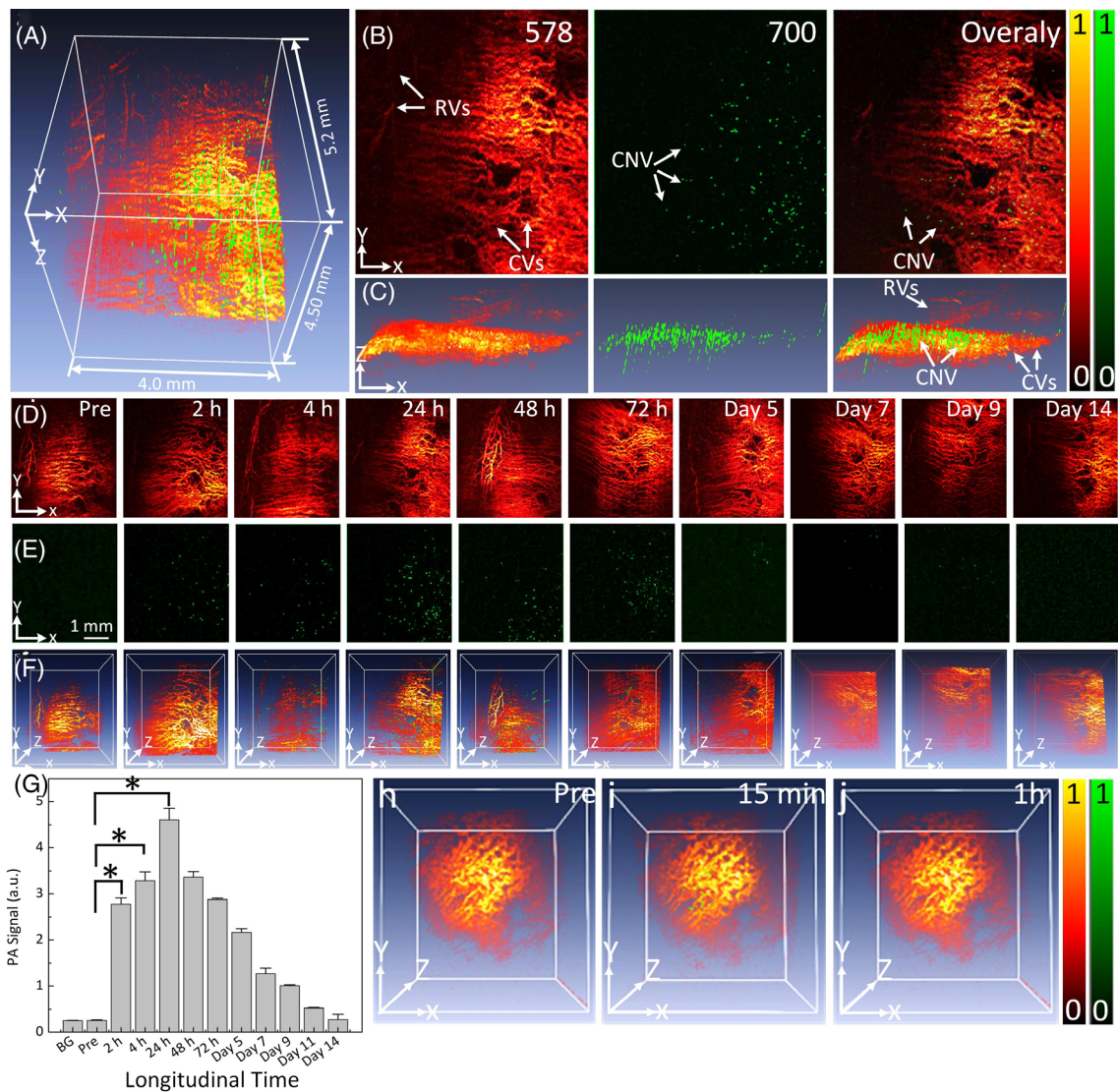


FIGURE 4 Longitudinal visualization of choroidal neovascularization in rabbit choroidal neovascularization (CNV) model: A, Merged 3D visualization photoacoustic microscopy (PAM) image of CNV acquired at two different excitation wavelengths of 578 (pseudo-red) and 700 (pseudo-green) nm (post 24 h). See Supplementary Visualization 1 for video representation. B, Horizontal (x-y) PAM image (post 24 h). C, Vertical (y-z) PAM image (post 24 h). Green color shows the position of ICG-RGD bound at CNV. (D-F) Longitudinal PAM images visualizing CNV obtained at the excitation wavelengths of 578 nm, D, and 700 nm, E, pre-injection of ICG-RGD, and after-injection at 2 h, 4 h, 24 h, 48 h, 72 h, day 5, 7, 9, 11 and 14 post-injection of ICG-RGD (0.4 mL, 2.5 mg/mL). White arrows show the location of CNV. CNV was not readily detectable in the PAM image before the injection of ICG-RGD. F, Overlay 3D PAM images. G, Graph of the measured PAM signal in the CNV. PA signal reached a peak PA amplitude at 24 h post-injection and gradually decreases over time. H-J, in vivo overlay 3D PAM images of CNV acquired at 578 and 700 nm pre- and post-administration of 0.4 mL ICG without conjugation with RGD at concentration of 2.5 mg/mL at 15 min, and 1 h. Pseudo-green color shows the location of CNV

injection. Three-dimensional volumetric rendering was performed and co-registered on the same image planes, allowing for visualization and determination of CNV from the surrounding microvasculature (Figure 4F). Furthermore, quantitative measurement PA amplitudes at the region of interest (ROI) at CNV showed that PA amplitudes rapidly increased and reached a peak at 24 h (Figure 4G). Then, the PAM amplitudes decreased over time. Compared to pre-injection, PA image contrast at

700 nm enhanced by 13-fold from 0.03 ± 0.001 a.u. pre-injection to 0.39 ± 0.03 a.u. at 2 h post-injection ($P < .001$). The peak PA amplitude within CNV was achieved at 24 h post-injection with the contrast enhancement of 15.7-fold ($PA_{\text{Signal}} = 0.47 \pm 0.03$ a.u.). This significant signal enhancement allows ICG to be a great contrast agent for PAM. To confirm the efficiency of ICG-RGD, a group of rabbits with CNV model was treated with ICG without conjugation with RGD as

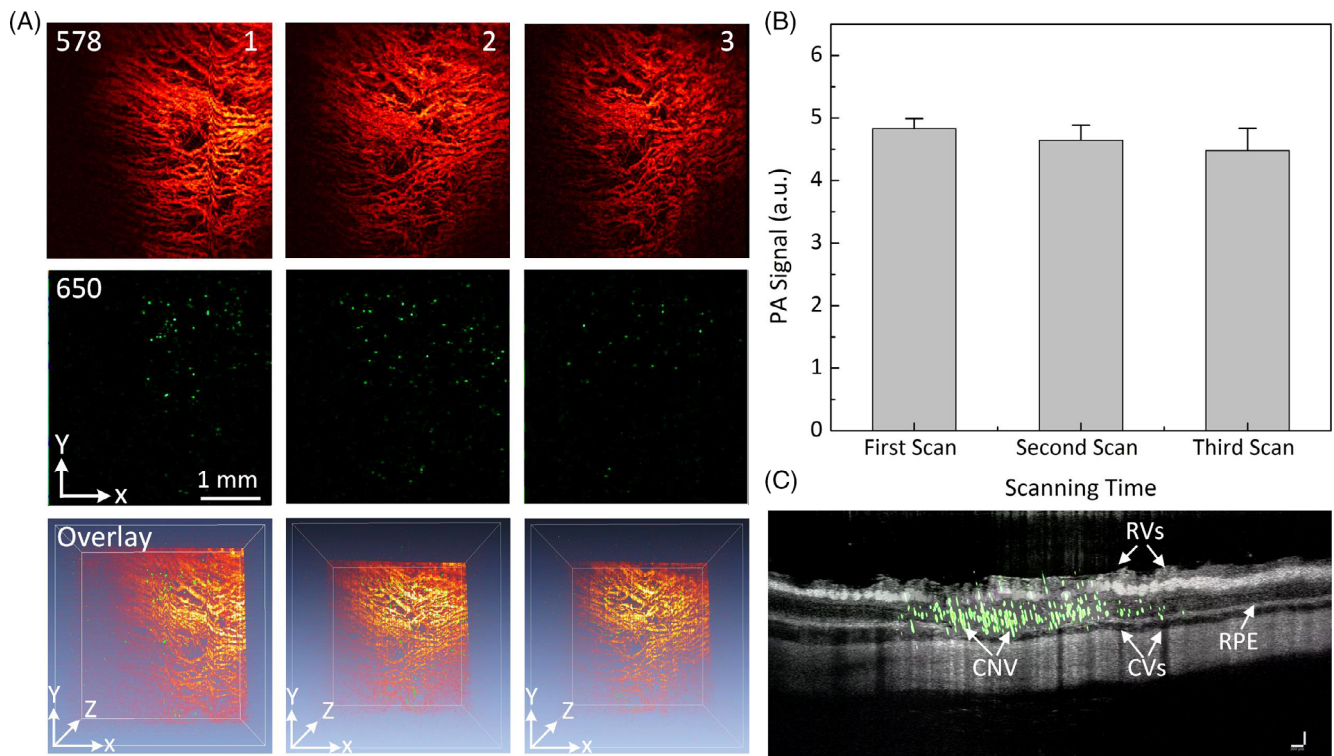


FIGURE 5 In vivo photostability evaluation: A, maximum intensity projection (MIP) photoacoustic microscopy (PAM) images achieved at 578 nm (top) and 650 nm (middle). The PAM images were acquired at three different scans at the same regions of interest (ROI) around choroidal neovascularization (CNV). The bottom images show the overlay 3D PAM images of CNV. White dotted arrows indicate the position of CNV. B, Graph of isolated PAM signal within CNV. The PAM signal varies by 8% between different scan acquisition times (i.e., 0.46 ± 0.02 (a.u.) for the first scan, and 0.42 ± 0.02 (a.u.) for the third scan, $P = .24 > .05$). C, Overlay B-scan OCT and PAM acquired at 700 nm. Pseudo-green color indicates the position of new developed CNV

shown in Figure 4H-J and Figure S4. The results show that the PAM signal intensity rapidly reduced after 15 min post-injection ($P < .002$, $n = 3$).

Although the laser energy used to induce PA signal is below the ANSI safety limit, the exposure time of about 65 s to achieve each PAM image could cause photobleaching [51]. To assess potential in vivo photobleaching, PAM images were implemented three times at the same selected scanning region (Figure 5). The image contrast did not change on the obtained PAM images (Figure 5A). Morphology of the retinal vessels and capillaries was clearly visible with high contrast. The estimated PA amplitudes show that the ICG PA amplitudes were stable with less than 5% difference in signal between the three scans (i.e., 0.15 ± 0.02 , 0.15 ± 0.01 , and 0.14 ± 0.02 (a.u.) for the first, second, and third scans, respectively). This illustrated the capacity for achieving long-term distinction between hemoglobin and CNV without a multi-dose injection requirement. To confirm the feasibility of multimodal PAM and OCT for enhanced visualization of CNV, an overly B-scan OCT and PAM images acquired at 700 nm on the same orthogonal imaging plane was implemented as shown in

Figure 5C. The result shows that CNV was located in sub-retinal space (pseudo-green color).

4.4 | In vivo immunostaining and toxicity analysis

To confirm the development of CNV, two group of the eye tissues were stained with SMA antibodies. The result shows clearly evidence of the location of newly developed CNV as shown in Figure 6 (brown colors). To investigate the biosafety of ICG-RGD, body weight analysis, serum blood tests, TUNEL assay, and histology were performed and evaluated in rabbits. The rabbit's weight of untreated group (control), treated with ICG without conjugation with RGD group and treated with ICG-RGD group were measured and recorded daily for up to 14 days after ICG-RGD injection. The body weight panel (Figure S5) shows no significant loss of body weight and appropriate weight gain in both the treated and untreated groups, illustrating that ICG and ICG-RGD did not cause severe systemic toxicity in rabbits. To evaluate the potential effect of ICG and ICG-RGD to the animal liver and kidney functions,

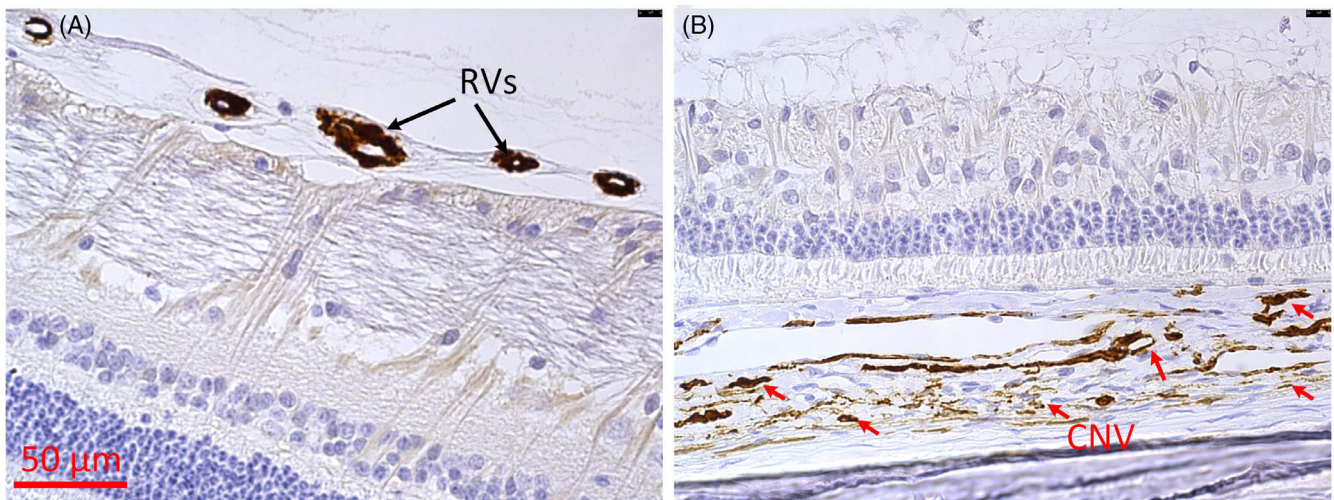


FIGURE 6 Immunohistochemistry analysis. Smooth muscle actin (SMA) staining showed the location of new developed choroidal neovascularization (CNV) (red arrows)

TABLE 1 Serum liver and kidney tests in rabbits demonstrating normal levels after ICG administration

Test	Unit	Normal range	Control group	ICG without RGD	ICG with RGD
Creatinine	mg/dL	0.5–2.6	1.80 ± 0.36	1.47 ± 0.67	1.57 ± 0.45
Albumin	g/dL	2.7–5	4.13 ± 0.40	3.83 ± 1.01	4.03 ± 0.61
Total protein	g/dL	5–7.5	6.63 ± 0.57	6.43 ± 0.70	6.13 ± 0.55
Alanine transaminase	U/L	25–65	60.67 ± 3.51	55.00 ± 7.00	42.67 ± 5.86
Total bilirubin	mg/dL	0.2–0.5	0.24 ± 0.08	0.38 ± 0.07	0.35 ± 0.06
Blood urea nitrogen	mg/dL	5–25	21.33 ± 3.06	20.00 ± 2.00	19.00 ± 2.65
Alkaline phosphatase	U/L	10–86	78.33 ± 6.51	78.00 ± 5.57	72.33 ± 12.90

Abbreviation: ICG, indocyanine green.

serum biochemistry testing was performed on each rabbit at 14 days post-injection (Table 1). Indices of alanine aminotransferase (ALT), creatinine (CRE), alkaline phosphatase (ALP), and blood urea nitrogen (BUN) values all remained within normal ranges, indicating no damage to liver or kidney function.

To visualize any potential structural damage caused by ICG-RGD, the eye, heart, kidney, lung, liver, and spleen were isolated, sliced, and stained with hematoxylin and eosin (H&E) and TUNEL assay (Figure 7). The H&E staining shows that no abnormal structures or cell morphology can be seen in any of the organs, indicating that ICG does not induce significant damage to any of these essential organs (Figure 7A,B). Apoptosis of the eye tissue and other vital organs was examined using TUNEL assay analysis (Figure 7C-E). No significant cells under apoptosis were observed on the TUNEL images, suggest no obvious ocular or systemic toxicity. Note that cell nuclei were stained with DAPI as indicated by blue colored fluorescence (Figure 7C) and green fluorescence

represents the apoptotic cells stained by FITC (Figure 7D).

5 | DISCUSSION

This study demonstrates that ICG-RGD can serve as an organic contrast agent for molecular PAM imaging to assess choroidal neovascularization in large animal eyes. The current study reveals that intravenous injection of ICG-RGD in rabbits led to PAM contrast in CNV increasing up to 15.7-fold compared to before the injection or injection with RGD targeting peptides alone. The PAM imaging results were further verified by OCT and planar fluorescence imaging. In addition, these results show that ICG-RGD are biocompatible and exhibit excellent photostability under pulsed laser illumination both in vitro and in vivo. Furthermore, ICG-RGD provides strong optical absorption spectrum in the NIR range, allows for evaluation the extravasation of ICG in CNV, and distinguishes

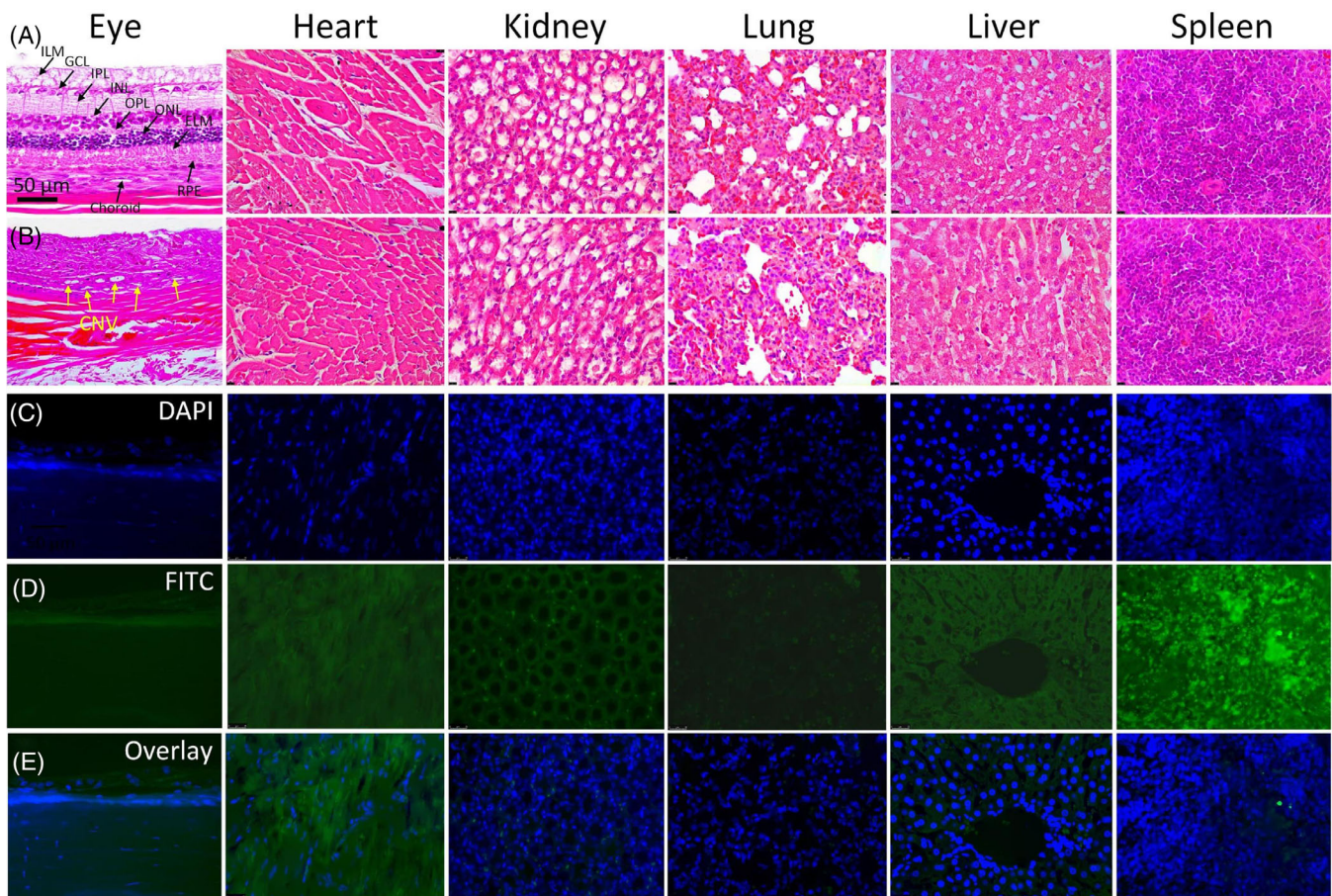


FIGURE 7 Histopathological and TUNEL assay analysis. Hematoxylin and eosin (H&E) images of eyes and organs obtained from control group, A and choroidal neovascularization (CNV) group, B. Cellular morphology appeared normal. C–E, TUNEL assay staining of treated tissues with ICG-RGD. Cell nuclei were stained with DAPI in blue fluorescent color, C. Cells under apoptosis or necrosis were stained with green fluorescent color from FITC, D. There is no evidence of apoptotic cells, indicating ICG-RGD did not induce systemic toxicity

the margin of CNV from surrounding vessels at a depth of $\sim 300\ \mu\text{m}$ by acquiring PAM images at different excitation wavelengths.

In previous studies, our group has described the feasibility of multimodal PAM and OCT imaging system as a potential platform to monitor various normal and abnormal retinal vasculature, such as RVs, CVs, RNV, and CNV with promising contrast and high resolution [23–25, 28, 52]. However, these healthy and abnormal vasculatures have strong PA signal caused by endogenous absorber like hemoglobin and melanin. Therefore, it is hard to distinguish them. To solve this problem, a semi-automated segmentation algorithm has been applied to classified between retinal vessels and retinal neovascularization as described by Nguyen et al. [23, 26] A major limitation of this method is that it is computationally time-consuming and not always accurate in discriminating newly developed neovascularization. In contrast, the advantage of the current study is that the

current custom-built multimodality imaging equipment with the assistance of exogenous contrast agents permits improved imaging of both structural and functional information of newly developed abnormal blood vessels in the eye which cannot be visualized using a single imaging system. In terms of visualization of microvasculature network and CNV, OCT and OCTA are widely applied in the clinic due to their real time capability and high resolution. Both OCT and OCTA can provide more details of different retinal layers. But one major difficulty of OCT and OCTA is that their penetration depth is limited by using scattering effect in biological tissue and high background signal, leading to difficulty visualizing the choroidal vasculature. Instead, OCT is used to describe choroidal thickness, which serves as a limited biomarker of disease. On the contrary, PAM offers several advantages relative to high spatial resolution and deep penetration based on the absorption efficiency of tissues. In addition, due to independent optical excitation

wavelength effect, spectroscopic PAM obtained at multiple wavelengths allows for selective visualization of CNV. By integration with OCT, both PAM and OCT images can be co-registered on the same orthogonal imaging plane, permitting enhanced identification of retinal pathogenesis.

Most previous studies on photoacoustic contrast agents have focused on inorganic materials such as gold nanoparticles due to their strong plasmonic absorption peak in the visible, NIR-I, and NIR-II windows. The optical characteristics of gold nanoparticles can be adjusted and controlled by changing the size, shape, or aggregation in biological tissues [38, 39, 53]. A study reported by Khoury et al. showed gold nanostars seeded from sphere gold nanoparticle with a size of 10 nm exhibited peak absorption at 650 nm [54]. Donnelly et al. have reported that gold spheres with a plasmonic peak at 520 nm were red-shifted to the NIR range when these nanoparticles aggregated in human mesenchymal stem cells (MSCs) [53]. However, a limitation of inorganic contrast agents is their large size, resulting in rapid clearance from the body after intravenous injection through the reticuloendothelial system (RES). Multi-dose injection may induce long-term toxicity to the animal [55]. In addition, most inorganic contrast agents are not approved by the FDA for clinical applications.

In contrast, ICG is an FDA-approved contrast agent that is commonly used in eye applications already. As a small molecule, it has unique properties and can be used for molecular targeting. In addition, untargeted molecular particles can be rapidly cleared from the body via urine, resulting in reduced toxicity to the animal. Although several studies have reported that fluorescent dyes are biodegradable and the acoustic signal significantly reduced under high power laser illumination due to photobleaching, our results demonstrate that ICG has a good temporal stability, biocompatibility *in vivo*, and photostability under pulsed laser illuminations for at least three scanning times (Figure 5) at a laser of about half of the ANSI safety limit. This allows for longitudinal evaluation of biological processes with a single injection. CNV was selectively discriminated from native vessels using multiple wavelengths. For example, a wavelength of 578 nm was used to visualize retinal vessels and CNV due to strong optical absorption of red blood cells within retinal vessels. A wavelength of 700 nm was applied to visualize the ICG. These images were co-registered on the same image plane, allowing for precise identification of the position as well as the margin of CNV. This offers several advantages when compared to previous studies [10, 23, 25, 26]. For example, Nguyen et al, Zhang et al and Li et al used a single wavelength of 578 nm to detect retinal neovascularization (RNV) and choroidal

neovascularization with high contrast image. However, these studies used a single excitation wavelength, resulting in difficulty in distinguishing RNV from healthy vessels. To classify RNV, the author used semi-automatic segmentation algorithm which may lose information from the target tissue or less precisely identify the margin of RNV. Importantly, these studies could not distinguish retinal capillaries and choriocapillaris before and after making the disease model. These unique characteristics made the conjugated ICG-RGD to be an ideal photoacoustic contrast agent for visualization of neovascularization *in vivo*.

Sharma et al. reported that some organic contrast agents suffered from poor photostability, insufficient *in vivo* stability, low quantum yield, and required multiple dose injection [56]. This may be caused by using high power of laser irradiation to produce sufficient PA signal, which can lead to photobleaching and increased degradation of fluorescence dyes. Elori et al. and Organisciak et al. have shown that the excitation laser light at high intensity may cause thermoacoustic damage or photochemical damage [47, 48]. In addition, longer duration of laser irradiation may also affect the stability of organic contrast agents. This study used a laser energy of ~80 nJ to excite the target tissue, which is half of the ANSI safety limit, possibly resulting in reduction in over-exposure of laser light and avoidance of thermoacoustic effects. By using optical scanning methods, the volumetric PAM image can be achieved within a minute, which is limited by the laser repetition rate of 1 kHz of the optical parametric oscillator (OPO). Compared to the scanning speed of 2.7 seconds described by Liu et al [57], the scanning speed of the current system can be further improved by switching to a higher laser repetition rate. The faster the scanning speed, the higher resolution and higher contrast can be achieved since the eye has very short fixation time of about 500 ms. [58] This will avoid unexpected motion artifacts, resulting in improved PAM image quality.

Another advantage is that ICG-RGD can target and stay within CNV for up to 5 days post-injection. This allows for longitudinal evaluation of CNV without re-injection of additional contrast agent. Multi-dose injection of photoacoustic contrast agent may cause side effects such as vomiting and nausea in up to 10% of patients and hypersensitivity reactions which can even result in anaphylaxis and death [59].

6 | CONCLUSIONS

This work investigates ICG-RGD as an organic molecular photoacoustic contrast agent for visualization of choroidal neovascularization in living rabbits. This study

demonstrates that ICG-RGD can show high-resolution, three-dimensional structure and margin of CNV as well as the differentiation of CNV from surrounding blood vessels. This could allow for improved understanding and diagnosis of neovascularization. ICG-RGD has strong optical absorption in the NIR window and good biostability and photostability that make it suitable for imaging CNV and microvasculature longitudinally. This work can provide valuable information to stimulate further study of CNV using photoacoustic molecular imaging.

ACKNOWLEDGMENTS

This study was supported by the National Eye Institute with grant number 1K08EY027458 (YMP) and Fight for Sight- International Retinal Research Foundation grant number FFSGIA16002 (YMP). This work was also supported by unrestricted departmental support from Research to Prevent Blindness and the University of Michigan Department of Ophthalmology and Visual Sciences. This research utilized the Core Center for Vision Research financed by the National Eye Institute grant number P30 EY007003. The authors thank Dr. Yuqing Chen and the Center for Advanced Models and Translational Sciences and Therapeutics (CAMTraST) at the University of Michigan Medical School for the generous donation of New Zealand rabbits, Dr. Thomas David for assistance with immunohistochemistry, and Dr. Lentz and Dr. Liu for assistance with the confocal microscope.

CONFLICT OF INTEREST

The authors declare no potential conflict of interest.

AUTHOR CONTRIBUTIONS


Van Phuc Nguyen designed, and employed the experiments, performed animal work, data analysis, in vitro characterization and in vivo OCT and PAM experiments, rendered three-dimensional volumetric visualization using Amira, and wrote the manuscript. Yanxiu Li conducted animal model. Jeff Folz synthesized contrast agents. Jessica Henry helped with histological analysis and monitored the animal post in vivo experiments. Wei Zhang assisted with maintenance of the imaging system. Xueding Wang was responsible for experimental planning, overall evaluation of the data and writing of the manuscript. Yannis M. Paulus contributed to organize and direct the project and wrote the manuscript. All authors executed a critical assessment of the data, and critical review of the manuscript.

DATA AVAILABILITY STATEMENT

The data that support the findings of this study are available from the corresponding author upon reasonable request.

ORCID

Van Phuc Nguyen  <https://orcid.org/0000-0001-7466-1483>

Yannis M. Paulus  <https://orcid.org/0000-0002-0615-628X>

REFERENCES

- [1] K. M. Gehrs, D. H. Anderson, L. V. Johnson, G. S. Hageman, *Ann. Med.* **2006**, *38*, 450.
- [2] W. L. Wong, X. Su, X. Li, C. M. Cheung, R. Klein, C. Y. Cheng, T. Y. Wong, *Lancet Glob. Health* **2014**, *2*, e106.
- [3] S. R. Flaxman, R. R. Bourne, S. Resnikoff, P. Ackland, T. Braithwaite, M. V. Cicinelli, A. Das, J. B. Jonas, J. Keeffe, J. H. Kempen, *Lancet Glob. Health* **2017**, *5*, e1221.
- [4] J. H. Meyer, P. P. Larsen, C. Strack, W. M. Harmening, T. U. Krohne, F. G. Holz, S. Schmitz-Valckenberg, *Exp. Eye Res.* **2019**, *184*, 162.
- [5] S. Kumar, Z. Berriochoa, A. D. Jones, Y. Fu, *J. Vis. Exp.* **2014**, *84*, e51061.
- [6] D. J. Feenstra, M. Selecic, N. Denk, S. Fauser, F. M. Drawnel, A. Jayagopal, *Exp. Eye Res.* **2019**, *180*, 122.
- [7] J. Birtel, M. Lindner, D. K. Mishra, P. L. Müller, D. Hendig, P. Herrmann, F. G. Holz, M. Fleckenstein, M. Gliem, P. Charbel Issa, *Clin. Experiment. Ophthalmol.* **2019**, *47*, 240.
- [8] V.-P. Nguyen, Y. Li, J. Henry, W. Zhang, M. Aaberg, S. Jones, T. Qian, X. Wang, Y. M. Paulus, *ACS Sens.* **2020**, *5*, 3070.
- [9] Y. M. Paulus, V. P. Nguyen, W. Qian, Y. Li, B. Liu, M. Aaberg, J. Henry, W. Zhang, X. Wang, *Invest. Ophthalmol. Vis. Sci.* **2020**, *61*, 3496.
- [10] Y. Li, W. Zhang, V. P. Nguyen, R. Rosen, X. Wang, X. Xia, Y. M. Paulus, *Exp. Eye Res.* **2019**, *186*, 107714.
- [11] S. Jeon, H. B. Song, J. Kim, B. J. Lee, R. Managuli, J. H. Kim, J. H. Kim, C. Kim, *Sci. Rep.* **2017**, *7*, 1.
- [12] H. Zhao, G. Wang, R. Lin, X. Gong, L. Song, T. Li, W. Wang, K. Zhang, X. Qian, H. Zhang, *J. Biomed. Opt.* **2018**, *23*, 046006.
- [13] V. P. Nguyen, Y. M. Paulus, *J. Imaging* **2018**, *4*, 149.
- [14] M. Xiao, C. Dai, L. Li, C. Zhou, F. Wang, *Ophthalmic Res.* **2020**, *63*, 271.
- [15] P. Zhang, A. Zam, Y. Jian, X. Wang, Y. Li, K. S. Lam, M. E. Burns, M. V. Sarunic, E. N. Pugh, R. J. Zawadzki, *J. Biomed. Opt.* **2015**, *20*, 126005.
- [16] R. W. Massof, F. W. Chang, *Vision Res.* **1972**, *12*, 793.
- [17] A. Hughes, *Vision Res.* **1979**, *19*, 569.
- [18] A. Hughes, *Vision Res.* **1972**, *12*, 123.
- [19] M. F. Deering, *ACM Trans. Graphics* **2005**, *24*, 649.
- [20] M. Adhi, J. S. Duker, *Curr. Opin. Ophthalmol.* **2013**, *24*, 213.
- [21] V. P. Nguyen, Y. Li, W. Zhang, X. Wang, Y. M. Paulus, *Sci. Rep.* **2020**, *10*, 1.
- [22] V. P. Nguyen, Y. Li, W. Qian, B. Liu, C. Tian, W. Zhang, Z. Huang, A. Ponduri, M. Tarnowski, X. Wang, *Sci. Rep.* **2019**, *9*, 1.
- [23] V. P. Nguyen, Y. Li, W. Zhang, X. Wang, Y. M. Paulus, *Biomed. Opt. Express* **2018**, *9*, 5915.
- [24] C. Tian, W. Zhang, A. Mordovanakis, X. Wang, Y. M. Paulus, *Opt. Express* **2017**, *25*, 15947.
- [25] W. Zhang, Y. Li, V. P. Nguyen, Z. Huang, Z. Liu, X. Wang, Y. M. Paulus, *Light* **2018**, *7*, 1.

- [26] V. P. Nguyen, Y. Li, M. Aaberg, W. Zhang, X. Wang, Y. M. Paulus, *J. Imaging* **2018**, *4*, 150.
- [27] C. Tian, W. Zhang, V. P. Nguyen, X. Wang, Y. M. Paulus, *J. Vis Exp* **2018**, *132*, 57135.
- [28] V. P. Nguyen, Y. Li, W. Zhang, X. Wang, Y. M. Paulus, *Sci. Rep.* **2019**, *9*, 1.
- [29] J.-W. Kim, E. I. Galanzha, E. V. Shashkov, H.-M. Moon, V. P. Zharov, *Nat. Nanotechnol.* **2009**, *4*, 688.
- [30] A. de la Zerda, S. Bodapati, R. Teed, S. Y. May, S. M. Tabakman, Z. Liu, B. T. Khuri-Yakub, X. Chen, H. Dai, S. S. Gambhir, *ACS Nano* **2012**, *6*, 4694.
- [31] A. De La Zerda, C. Zavaleta, S. Keren, S. Vaithilingam, S. Bodapati, Z. Liu, J. Levi, B. R. Smith, T.-J. Ma, O. Oralkan, *Nat. Nanotechnol.* **2008**, *3*, 557.
- [32] A. de la Zerda, Z. Liu, S. Bodapati, R. Teed, S. Vaithilingam, B. T. Khuri-Yakub, X. Chen, H. Dai, S. S. Gambhir, *Nano Lett.* **2010**, *10*, 2168.
- [33] K. Yang, L. Zhu, L. Nie, X. Sun, L. Cheng, C. Wu, G. Niu, X. Chen, Z. Liu, *Theranostics* **2014**, *4*, 134.
- [34] G. Ku, M. Zhou, S. Song, Q. Huang, J. Hazle, C. Li, *ACS Nano* **2012**, *6*, 7489.
- [35] O. Ogunlade, J. O. Ho, T. L. Kalber, R. E. Hynds, E. Zhang, S. M. Janes, M. A. Birchall, C. R. Butler, P. Beard, *Photoacoustics* **2019**, *13*, 76.
- [36] H. Kim, P. M. Van Phuc Nguyen, M. J. Jung, S. W. Kim, J. Oh, H. W. Kang, *Oncotarget* **2017**, *8*, 113719.
- [37] G. P. Luke, S. Y. Nam, S. Y. Emelianov, *Photoacoustics* **2013**, *1*, 36.
- [38] J. Weber, P. C. Beard, S. E. Bohndiek, *Nat. Methods* **2016**, *13*, 639.
- [39] Q. Fu, R. Zhu, J. Song, H. Yang, X. Chen, *Adv. Mater.* **2019**, *31*, 1805875.
- [40] A. P. Jathoul, J. Laufer, O. Ogunlade, B. Treeby, B. Cox, E. Zhang, P. Johnson, A. R. Pizzey, B. Philip, T. Marafioti, *Nat. Photonics* **2015**, *9*, 239.
- [41] Y. Jiang, P. K. Upputuri, C. Xie, Y. Lyu, L. Zhang, Q. Xiong, M. Pramanik, K. Pu, *Nano Lett.* **2017**, *17*, 4964.
- [42] Y. Zhang, M. Jeon, L. J. Rich, H. Hong, J. Geng, Y. Zhang, S. Shi, T. E. Barnhart, P. Alexandridis, J. D. Huizinga, *Nat. Nanotechnol.* **2014**, *9*, 631.
- [43] V. P. Nguyen, S. Park, J. Oh, H. Wook Kang, *J. Biophotonics* **2017**, *10*, 1053.
- [44] C. Kim, K. H. Song, F. Gao, L. V. Wang, *Radiology* **2010**, *255*, 442.
- [45] L. A. Yannuzzi, *Am. J. Ophthalmol.* **2011**, *151*, 745.
- [46] <https://www.lia.org/store/product/ansi-z1361-2014-safe-use-lasers-electronic-version>. **2007**.
- [47] T.-R. Kuo, V. A. Hovhannisyan, Y.-C. Chao, S.-L. Chao, S.-J. Chiang, S.-J. Lin, C.-Y. Dong, C.-C. Chen, *J. Am. Chem. Soc.* **2010**, *132*, 14163.
- [48] D. T. Organisciak, D. K. Vaughan, *Prog Retin Eye Res.* **2010**, *29*, 113.
- [49] T. Ma, X. Zhang, C. T. Chiu, R. Chen, K. K. Shung, Q. Zhou, S. Jiao, *J. Biomed. Opt.* **2014**, *19*, 016015.
- [50] S. Petrus-Reurer, H. Bartuma, M. Aronsson, S. Westman, F. Lanner, H. André, A. Kvanta, *Invest. Ophthalmol. Vis. Sci.* **2017**, *58*, 1314.
- [51] J. Laufer, A. Jathoul, M. Pule, P. Beard, *Biomed. Opt. Express* **2013**, *4*, 2477.
- [52] V. P. Nguyen, Y. Li, J. Henry, R. Rosen, M. Aaberg, W. Zhang, X. Wang, Y. M. Paulus in Integrated photoacoustic microscopy and optical coherence tomography image-guided laser induced branch retinal vein occlusion in living rabbits, International Society for Optics and Photonics, City, **2019**, pp.1087104.
- [53] E. M. Donnelly, K. P. Kubelick, D. S. Dumani, S. Y. Emelianov, *Nano Lett.* **2018**, *18*, 6625.
- [54] C. G. Khoury, T. Vo-Dinh, *J. Phys. Chem. C* **2008**, *112*, 18849.
- [55] J. D. Bartlett, T. G. Slusser, A. Turner-Henson, K. P. Singh, J. A. Atchison, D. J. Pillion, *J. Ocul. Pharmacol. Ther.* **1994**, *10*, 101.
- [56] P. Sharma, S. Brown, G. Walter, S. Santra, B. Moudgil, *Adv. Colloid Interface Sci.* **2006**, *123*, 471.
- [57] W. Liu, H. F. Zhang, *Photoacoustics* **2016**, *4*, 112.
- [58] D. Robinson, *J. Physiol.* **1964**, *174*, 245.
- [59] M. Lopez-Saez, E. Ordoqui, P. Tornero, A. Baeza, T. Sainza, J. Zubeldia, M. Baeza, M. L. Baeza, *Ann. Alergy Asthma Immunol.* **1998**, *81*, 428.

SUPPORTING INFORMATION

Additional supporting information may be found online in the Supporting Information section at the end of this article.

How to cite this article: Nguyen VP, Folz J, Li Y, et al. Indocyanine green-enhanced multimodal photoacoustic microscopy and optical coherence tomography molecular imaging of choroidal neovascularization. *J. Biophotonics*. 2021;14:e202000458. <https://doi.org/10.1002/jbio.202000458>